NANO REVIEW

Self-organised synthesis of Rh nanostructures with tunable chemical reactivity

**F. Buatier de Mongeot · A. Toma · A. Molle ·
S. Lizzit · L. Petaccia · A. Baraldi**

Abstract Nonequilibrium periodic nanostructures such as nanoscale ripples, mounds and rhomboidal pyramids formed on Rh(110) are particularly interesting as candidate model systems with enhanced catalytic reactivity, since they are endowed with steep facets running along non-equilibrium low-symmetry directions, exposing a high density of undercoordinated atoms. In this review we report on the formation of these novel nanostructured surfaces, a kinetic process which can be controlled by changing parameters such as temperature, sputtering ion flux and energy. The role of surface morphology with respect to chemical reactivity is investigated by analysing the carbon monoxide dissociation probability on the different nanostructured surfaces.

F. Buatier de Mongeot · A. Toma · A. Molle
Dipartimento di Fisica, Università di Genova and CNISM, Via Dodecaneso 33, 16146 Genova, Italy

F. Buatier de Mongeot
e-mail: buatier@fisica.unige.it

S. Lizzit · L. Petaccia
Sincrotrone Trieste S.C.p.A, S.S. 14 Km 163.5, 34012 Trieste, Italy

S. Lizzit
e-mail: lizzit@elettra.trieste.it

A. Baraldi
Physics Department and Center of Excellence for Nanostructured Materials, Trieste University, Via Valerio 2, 34127 Trieste, Italy

A. Baraldi (✉)
Laboratorio TASC INFM-CNR, S.S. 14 Km 163.5, 34012 Trieste, Italy
e-mail: alessandro.baraldi@elettra.trieste.it

Introduction

The control of the atomic step distribution of clusters and nanostructures is of utmost importance in determining, among others, their magnetic [1], electrical, and catalytic properties. Recent experiments and theoretical models have tried to elucidate the atomistic details underlying the enhanced surface chemical reactivity of these active sites of transition metals (TM). Among these, extensive studies of carbon monoxide chemisorption on TM surfaces have been a valuable resource for the development of surface chemistry. CO, a toxic molecule contained in the automotive exhaust gases, is object of conversion via catalytic oxidation reduction [2]. The carbon monoxide dissociation process is a key step in the syngas reaction which is widely used in the industrial chemistry [3] for methane formation via the $CO + 3H_2 \rightarrow CH_4 + H_2O$ reaction or in the Fisher–Tropsch reaction [4] where CO and H_2 are transformed in hydrocarbons via the $nCO + 2nH_2 \rightarrow C_nH_{2n} + nH_2O$ ($n > 2$) reaction. This, along with the basic interest in understanding the mechanism involved in dissociative adsorption of heteroatomic molecules, has placed CO in the list of the most extensively studied adsorbed molecules [5]. The room temperature interaction of CO with transition metal surfaces can be divided in two main groups. The first includes transition metals from the left side of the periodic table, such as Fe, W and Mo, which adsorb CO dissociatively, while the second is composed by elements from the right side of the periodic table such as Co, Ni, Ru, Rh, Pd, Ir and Pt, which tend to adsorb CO molecularly.

However CO dissociation can also occur on the latter metals, in particular Ru, Rh and Ni, under defined temperature, pressure and surface structural conditions, which allow the molecules to overcome the activation barrier for dissociation. Detailed experimental and theoretical investigations performed in the last 15 years report that the chemical reactivity strongly increases on corrugated surfaces and that CO dissociation is sensitive to the structure of the substrate: steps and kinks drastically modify the reaction paths on solid surfaces and appear to be the most active sites for the C–O bond breaking [6, 7].

To this respect a general relation between the chemical reactivity, the d-band center and thus the coordination number of surface atoms, has been established [8–10]: the lower the coordination number of TM surface atoms, the smaller the local bandwidth and the higher the d-band centre position relative to the Fermi level for metals like Rh with a more than half-filled d band. Detailed calculations [11] based on Density Functional Theory (DFT) report reaction barriers for the CO → C + O reaction which strongly decrease when passing from the flat Rh(111) surface (E_a = 1.17 eV) to steps (E_a = 0.30 eV) and kinks (E_a = 0.21 eV). Coordination numbers of these metal atoms range from n = 9, to n = 7 (steps) and n = 6 (kinks). Other DFT calculations by Mavrikakis et al. [12] have shown that the energy of the transition state for CO dissociation on Rh(211) is about 120 kJ/mol lower than on the (111) terrace. In this case the coordination of the atoms at the steps is 7.

Experimental investigations indeed report that CO dissociation is negligible on close packed (111), (110) and (100) Rh surfaces [13] and that it increases on stepped (211) [12], (210) Rh substrates [14]. The dissociation process has been also extensively studied on Rh nanoparticles supported on thin Al_2O_3 films grown on a NiAl(110) single crystal, as a function of particle size [15, 16]. Maximum activity has been measured for particles containing about 1000 atoms, but the nature of the active sites was not explained.

It is a natural consequence of these detailed surface science studies to expect that promotion, enhancement, steering and control of CO dissociation can be reached by simply tuning surface morphology with the purpose of changing the density of reaction centers. Recently, it has been found that it is possible to tune the morphology and step distribution of a crystalline Rh(110) substrate by controlled exposure to a beam of noble gas ions: Xe ion irradiation at few hundreds eV leads to the formation of nonequilibrium periodic nanostructures such as nanoscale ripples, oriented either along [001] or [1–10] directions, mounds, and unexpected rhomboidal pyramids (RP) [17, 18]. The latter nanostructures are particularly interesting as candidate model systems for testing catalytic reactivity,

since they are endowed with steep facets running along nonequilibrium directions, exposing a high density of undercoordinated atoms.

Morphological characterisation of nanostructures

The irradiation of transition metal surfaces with an energetic noble ion beam yields the self-organization of a great number of nanoscaled patterns. They originate from the surface instability induced by the ion sputtering as well as from the diffusion balance among the removed adatoms.

Here we show how the sputtering parameters, i.e. the substrate temperature T, the ion flux f, the impact energy ε may influence the structural features of the surface patterns in the case of a Rh(110) surface sputtered with energetic Xe ions at an incidence angle of 15° from the surface normal.

Experimental: Spot Profile Analysis-LEED

Structural characterization of nanoscale surfaces was performed by in situ spot profile analysis low energy electron diffraction (SPA-LEED) which provides information on large surface area by integrating the diffraction signal on the scale of the electron beam size (about 0.1 mm). As a general consideration on the electron diffraction from sample crystal surfaces, constructive (in-phase) and destructive (anti-phase) interference from the exposed terraces are identified respectively by integer and half-integer values of the vertical scattering phase $S_z = k_z d/2\pi$, k_z and d being the vertical momentum transfer and the monoatomic step height [19].

Taking benefit from an instrumental transfer width of about 0.1 μm (i.e. the maximum lateral extension over which the electron wavelength is coherent), the SPA-LEED provides a high resolution magnification on the diffraction spot features. In this way we can investigate the facet distribution of the nano-structured entities and the dominant Fourier modes in the height–height correlation of the surface profile [17]. While a selective faceting can be recognized from the emergence of a couple of S_z dependent Bragg peaks at both sides of the central (0,0) Bragg peak, the presence of a lateral correlation Λ between the surface nanostructures is displayed as an additional, S_z independent, satellite splitting of the near to in-phase spot profile (S_z close to integer values). Figure 1 displays a three dimensional (3D) plot of the (0,0) spot profile for a one dimensional (1D) ripple-like pattern on the parallel momentum transfer plane $K_{\langle 001 \rangle} - K_{\langle 1-10 \rangle}$. The image was recorded in a scattering phase condition such that both couples of satellites can be envisioned (see also the dashed lines in the contour plot of the spot profile reported in the inset). As mentioned above, the inner couple of satellites is
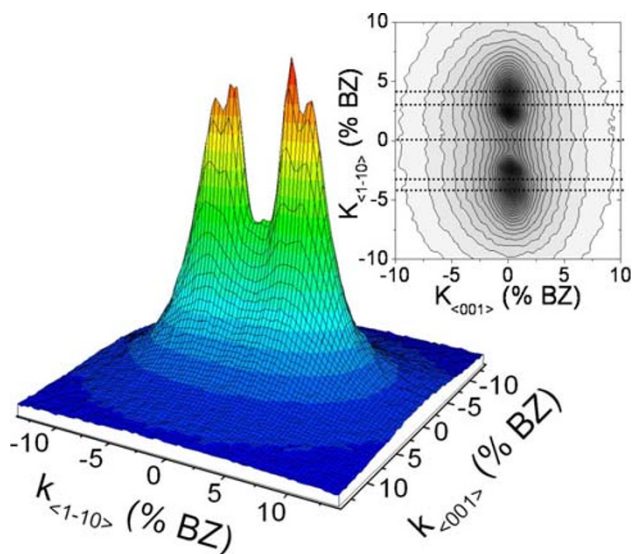
Fig. 1 3D plot of the (0,0) diffraction peak acquired under near-in phase conditions ($S_z = 2.1$) by means of SPA-LEED for a rippled surface. The multiple satellite splitting indicates the presence of a well defined lateral correlation and facets (see text for details). Inset: 2D contour plot of the spot profile (the dashed lines indicate the position of the satellites). Reproduced from Ref. [18]

Fig. 2 Out-of-phase Spot Profile ($S_z = 2.2$) after sputtering at: T = 450 K (**a**), T = 500 K (**b**), and T = 550 K (**c**). The axis scale is expressed in % of Brillouin Zone referred to the short side of the reciprocal surface cell. Panel (**b**) and (**c**) are reproduced from Ref. [17]. (d) AFM topography corresponding to an HTR morphology equivalent to panel (c) on a 600 × 600 nm scale. Inset: FFT contour profile of the AFM image. ε = 1000 eV

due to the average periodicity of the rippled corrugations whereas the outer couple, whose splitting turns out to be linearly dependent on the scattering phase, reflects the diffraction from the slope selected ripple facets. Therefore the out-of-phase spot profiles, i.e. far from integer values of vertical scattering phase S_z, can be effectively regarded as maps of the average facet slopes which have been selected during the surface structuring/re-organization upon ion irradiation.

The role of the substrate temperature during ion irradiation is reported in Fig. 2. Each spot profile is linked to a peculiar morphology obtained by patterning the initially flat Rh(110) substrate (terrace width above 60 nm) with Xe ion beam with ε = 1000 eV at three different temperatures, 450, 500 and 550 K. A ripple corrugation elongated in the ⟨001⟩ direction (Low Temperature Ripple-LTR motif) is inferred from the spot profile in Fig. 2a, measured in a nearly out-of-phase condition ($S_z \approx 2.1$), with a lateral periodicity of the ripple $\Lambda = 2\pi/q_0 = (15.8 \pm 0.5)$ nm. The outer satellites are due to the presence of regular step arrays (and facets) along the ⟨001⟩ direction. When moving towards an out-of-phase diffraction point, the outer satellites dominate the diffraction pattern and their splitting increases linearly with S_z giving the facet slope $\xi_{\langle 1-10 \rangle} = 10.5° \pm 2.6°$ [20]. Increasing the temperature up to 550 K (Fig. 2c) the spot profile apparently presents some qualitative affinities—e.g. twofold symmetry, satellite splitting—with the LTR case in Fig. 2a apart from a rotation of 90° in the reciprocal space which indicates a
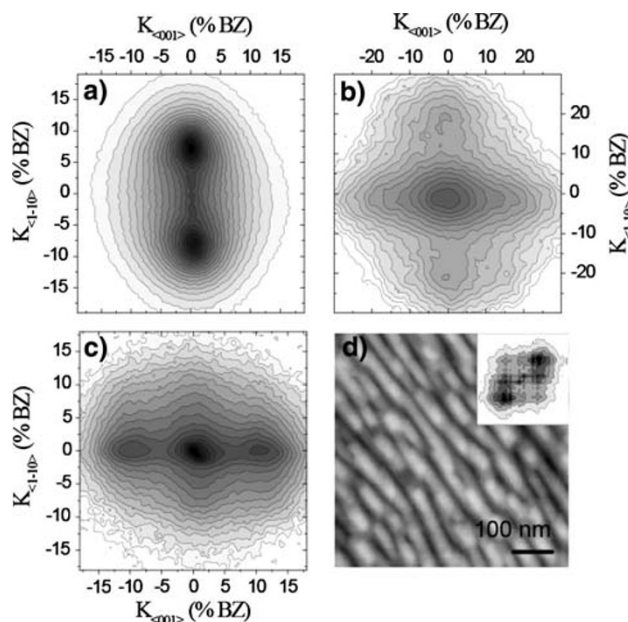
ripple orientation along the ⟨1 − 10⟩, with facets and dominant steps in the same direction (High Temperature Ripples pattern). The real space morphology corresponding to the HTR pattern is displayed in the surface topography in Fig. 2d taken by Atomic Force Microscopy (AFM). The AFM image elucidates that the High Temperature Ripples (HTR) pattern consists of almost 1D corrugations roughly elongated in the ⟨1 − 10⟩ surface direction with a high degree of lateral order ($\Lambda = 60 \pm 2$ nm) as confirmed by well defined couple of first order correlation peaks resulting in the fast Fourier transform diagram shown in the inset. Therefore the temperature increase from 450 K to 550 K gives rise to a rotation of the ripples by 90°.

If the intermediate temperature of 500 K is chosen, the out-of-phase diffraction profile in Fig. 2b is modified in a cross-like shape originating from the coexistence of high symmetry ⟨1–10⟩ and ⟨001⟩ oriented facets which bound the sides of the rectangular shaped islands constituting the Round Mouth (RM) pattern. The arrangement of the RM pattern actually appears as the interplay between the majority bounding steps in the two extreme cases of the LTR and HTR patterns. The temperature sequence of the surface patterns formed during Rh(110) sputtering is similar to that observed in the case of Ag(110) [21] and Cu(110) [22], apart from a shift to higher temperatures consistent with the larger diffusion barriers for Rh(110).
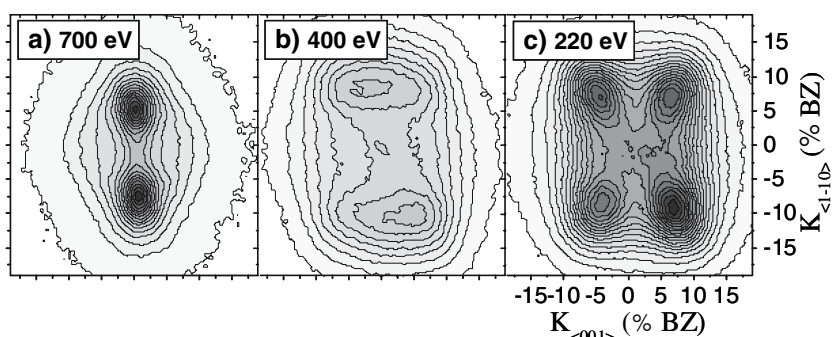
The observation of the RM pattern was also reported in the homoepitaxial growth on Ag(110) [20].

The effect of the impact energy ε of the impinging Xe ions on the SPA-LEED pattern is shown in Fig. 3 where the out-of-phase ($S_z \approx 2.2$) SPA-LEED plots related to three values of the impact energy, 700, 400 and 220 eV are reported. At $\varepsilon = 700$ eV both the two-fold symmetry and the 1D character of the spot profile identifies a LTR motif with $\Lambda_{\langle 1-10 \rangle} = (15.0 \pm 0.5)$ nm and $\xi_{\langle 1-10 \rangle} = 10.8° \pm 2.5°$ (Fig. 3a), qualitatively similar to that of Fig. 2a, i.e. with ripple corrugations bound by $\langle 001 \rangle$ oriented steps and facets. The LTR pattern undergoes a loss of the lateral correlation between adjacent corrugations and of the structural order in the facet arrangement upon a slight reduction of the impact energy to $\varepsilon = 400$ eV as demonstrated by the broadening of the spot profile in Fig. 3b. With $\varepsilon = 220$ eV, the (00) diffraction spot splits in fourfold fashion, with satellites along low symmetry directions (see the four-lobe shaped spot profile in Fig. 3c).

A quantitative description of the new structure at the atomistic level is reported in Fig. 4. Figure 4a shows a sequence of diffraction patterns of the (00) spot, acquired at increasing S_z values after patterning the Rh(110) surface with Xe ions with $\varepsilon = 220$ eV at T = 450 K. Moving away from the condition of constructive interference ($S_z = 2$), the (0,0) peak dissolves into four equivalent sub-peaks with a mutual separation linearly proportional to the variation of the scattering phase. Therefore the nature of the sub-peaks can be directly ascribed to the formation of facets with non-conventional bounding step-edges. The orientation of the majority steps has been deduced by plotting the satellite position in the parallel momentum transfer plane ($K_{\langle 001 \rangle} - K_{\langle 1-10 \rangle}$), for different values of S_z (see the diagram in Fig. 4b). The majority steps constituting the facets turn out to be placed along the diagonal axis of the surface unit cell, i.e. the $\langle 1-12 \rangle$ directions of low symmetry which form an angle $\xi_{\langle 1-12 \rangle} \approx 34.5°$ with respect to the $\langle 001 \rangle$ axis (see the inset). The average tilt angle of the facets with respect to the (110) reference plane is derived by linear extrapolation of the satellite splitting in a completely destructive interference condition. The method is
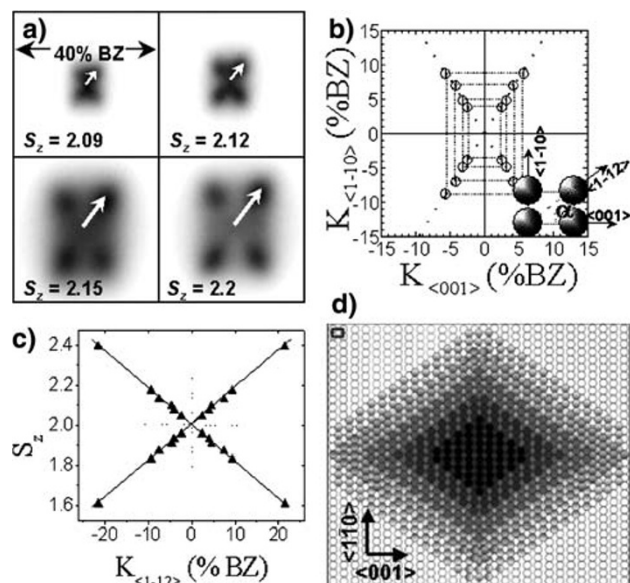

Fig. 4 Structural characterization of the RP state: (**a**) sequence of the (00) spot profile at several vertical scattering phases S_z (the arrows indicate the position of one satellite); (**b**) satellite position in the parallel momentum transfer plane $K_{<1-10>} - K_{<001>}$ using S_z as a parameter; (**c**) plot of the satellite splitting as a function of S_z; (d) simplified cartoon of a RP island with step edges running along well-defined $<1-12>$ directions. Darker colors correspond to topmost layers. The figure is reproduced from Ref. [17]

shown in Fig. 4c where from the plot of the satellite splitting versus the scattering phase S_z a facet slope $\alpha = 11° \pm 2°$ and terrace width $\Gamma \approx 6.6$ Å are derived. As sketched in the hard sphere cartoon model of Fig. 4d, the terrace width is compatible with three lattice constant along the $\langle 1-10 \rangle$ close-packed atomic rows. The four-lobe diffraction profile can thus be related to real-space objects bound by four dominant facets pointing towards low symmetry directions, consistently with the presence of rhomboidal pyramids (RP) on the surface. The $\langle 1-10 \rangle$ lateral periodicity $\Lambda \approx 14.7$ nm, deduced from near-in-phase measurements, definitely supports the identification of the four-lobe spot profiles in Fig. 4a with an ordered pattern of RP mounds in the real space. These observations allow us to unambiguously identify the novel morphological state with

the RP state theoretically predicted in Ref. [23]. However, since the latter model is expressed in terms of dimensionless parameters, the experiment should elucidate how the experimental variables determine the transition between the various morphological states.

The role of the impact energy in the surface nano-structuring and the concomitant formation of the RP pattern have been also generalized to the Cu(110) surface [17, 18] provided that the substrate temperature was properly rescaled because of the different diffusion barriers for the two transition metal surfaces. It is just the case of the Cu(110) surface erosion which enables us to discriminate two contrasting trends in the energy dependence of the correlation length Λ and of the facet slope α of the relevant surface patterns within the energy range from 200 eV to 3,000 eV (see the diagram in Fig. 5). For 200 eV < $\varepsilon \leq$ 500 eV, Λ follows a steep monotonic decrease with the energy, whereas, above 500 eV, this behaviour is reversed. An opposite trend is observed for the slope of the relevant surface structures: first increasing ($\varepsilon \leq$ 500 eV) and then decreasing ($\varepsilon >$ 500 eV). The observation of well-distinguished behavior for Λ and α in the considered range of impact energies is strictly related to the structural transition from the RP phase to the LTR phase as the critical energy of 500 eV is crossed. This argument is supported by the observation of different facets which characterize the two structural phases, as reported in the energy dependence of the facet slope in Fig. 5. For clarity, the RP pattern develops facet slopes extended along the $\langle 1-11 \rangle$ real space direction, having majority steps along the $\langle 1-12 \rangle$, as deduced from the analysis in Fig. 4, and linearly
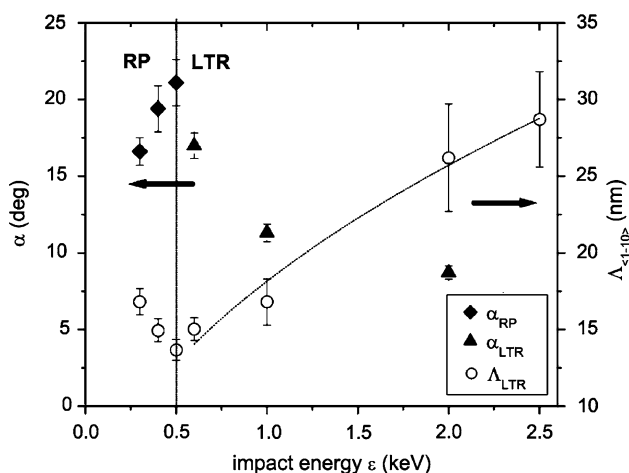
increasing with the energy. Conversely, the LTR morphology consists of 1D corrugations elongated in the $\langle 001 \rangle$ direction with roof-top facets through the perpendicular $\langle 1-10 \rangle$ direction with decreasing slope for increasing energy.

The emergence of the LTR phase, for $\varepsilon >$ 500 eV, can be rationalized from an atomistic viewpoint based on Scanning Tunneling Microscopy (STM) investigations of single ion impacts on the Ag(001) and Pt(111) surfaces [24, 25]. In those studies vacancy clusters with size of several nanometers are generated by the ion collisions and are coupled to several surrounding clusters which consist of the displaced adatoms. Within the crater width every correlation is reasonably suppressed due to the locally hyper-thermal collision transient. The ascending character of the wavelength, observed in our data, can be thus regarded as a consequence of the increasing crater radius with the impact energy in agreement with molecular dynamics simulations [26]. The LTR state arises then from the onset of impact-induced ''hot spots'' involving a local surface melting in the volume around the collision point [25, 27]. This assumption is corroborated by the slope relaxation intervening at higher impact energy (see Fig. 5), i.e. when the thermal spike affects wider areas of the surface [28]. In addition, the loss of correlation for higher energy can be reasonably associated either to the stronger excitation transferred to the surface atoms from the impinging ions or to an increase of the lateral extension of the impact crater.

Let's now consider the decrease of the correlation length Λ of the RP state, when ε ranges from 200 eV to 500 eV. Again, from the atomistic approach, this behavior can be understood in terms of the actual damage produced by the ion impact. Contrary to the ''thermal spike'' picture applied to the LTR case, decreasing the impact energy may have a critical role in the concentration of mobile defects at the topmost surface layer. This argument is supported by the observation of a monotonic increase of the adatom yield with the energy on the Pt(111) surface in the energy range 40–10,000 eV, as follows from STM analysis of single ion impacts [25] and from molecular dynamics simulations [26]. The role of the impact energy is effectively analogous to that of the deposition flux in homo-epitaxial growth: increasing the energy yields a higher concentration of mobile defects (mainly adatoms), which rearrange in stable nuclei after the ion impact. The higher density of stable nuclei on the surface and the lower correlation length between them, can explain the behavior of Λ in the RP regime (Fig. 5).

These arguments—especially the tendency of the impact energy to act as the deposition flux—find a phenomenological confirmation in the comparative study shown in Fig. 6, where the surface patterns induced on Cu(110) surface by Xe ion beam are investigated as a function of the

Fig. 5 Energy dependence of the correlation length Λ along the $\langle 1-10 \rangle$ (open circles) and of the facet slope (rhomboidal points refer to RP facets, triangular point to LTR facets) of the surface structures. The vertical line marks the border between the RP and the LTR regime (see text for details). The line between dots is a guide to the eye. The figure is reproduced from Ref. [18]

Fig. 6 Out-of-phase diffraction maps ($S_z = 1.88$) after ion irradiation of Cu(110). (**a**), (**b**), (**c**) Temperature dependence after dosing at $\varepsilon = 400$ eV, $f = 1.5$ ML/min for a total fluence of 21 ML. (**d**), (**e**), (**f**) Flux dependence after dosing at $\varepsilon = 400$ eV and T = 230 K for a total fluence of 21 ML. (**g**), (**h**), (**i**) Energy dependence for irradiation at the flux f = 1 ML/min and at T = 230 K for a total fluence of 45 ML. The figure is reproduced from Ref. [17]
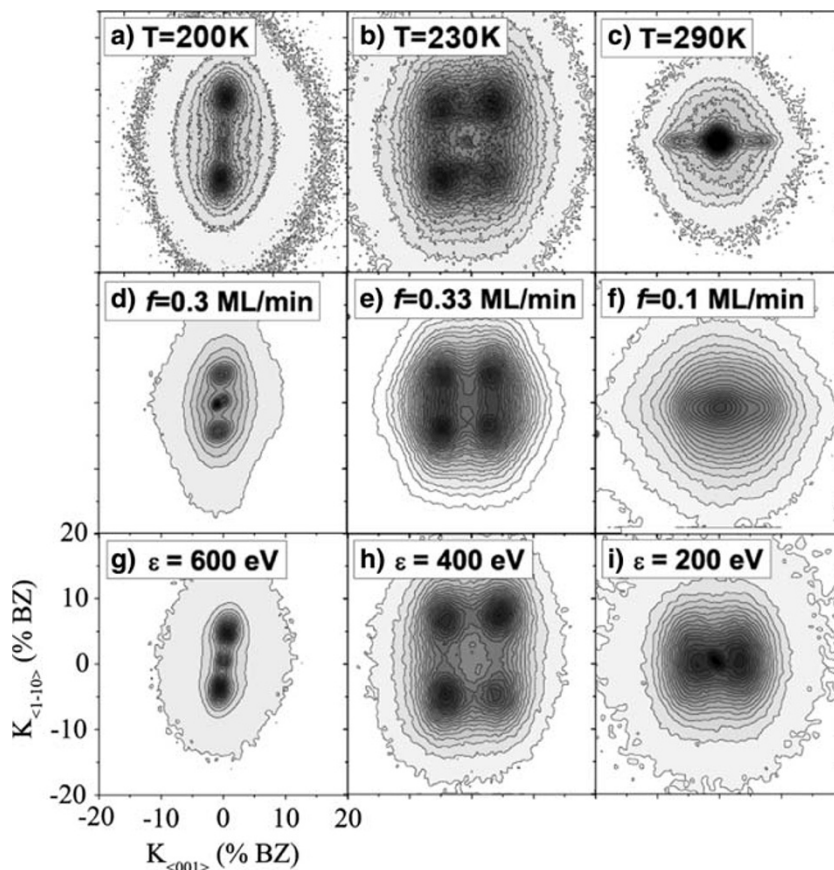
substrate temperature T, the ion flux f and impact energy ε, as for Rh(110). In Fig. 6a–c the Xe sputtering temperature dependence of the surface morphology is explored at fixed energy $\varepsilon = 400$ eV: the panels show a set of out-of-phase spot profiles for the three temperatures of 200, 230 and 290 K after exposing the Cu(110) surface to a Xe ion beam. Sputtering at T = 200 K (Fig. 6a) generates a LTR pattern. At the intermediate temperature T = 230 K (Fig. 6b) the spot profile acquires the fourfold symmetry, indicating that the RP state is formed. Finally, increasing the temperature to 290 K (Fig. 6c), the transition towards the HTR configuration is observed. This sequence confirms that also for Cu(110) the reduction of the energy below 400 eV is mandatory to access the RP pattern. On the other hand, the strong dependence of the pattern on the substrate temperature suggests that the evolution of the RP state is mainly dictated by the kinetics of thermally activated diffusion processes involving the adatoms displaced after the ion collision, rather than by the details of the hyperthermal ion-surface collision transient.

Since the ion flux f defines the relaxation time between two subsequent collision events, a morphological variation of the surface structure similar to that observed in the T dependence of Fig. 6a–c, is expected even for different ion flux f. This is shown in Fig. 6d–f: here the out-of-phase

diffraction maps of the (00) spot are reported for three different fluxes at $\varepsilon = 400$ eV and T = 230 K. Sputtering at a relatively low flux ($f = 0.1$ ML/min—Fig. 6f) results in a faint HTR pattern; in the intermediate range ($f = 0.3$–1 ML/min—Fig. 6e) the RP state emerges, while further increasing the flux ($f = 3$ ML/min—Fig. 6d) the transition to a well-resolved LTR state occurs. From this it can be concluded that, *the decrease of the ion flux* on the surface morphology corresponds to *the increase of the substrate temperature*, further confirming the kinetic and diffusive mechanisms underlying the pattern formation.

According to the atomistic approach proposed for the discussion of Fig. 5, a further question which has to be addressed is the role of the ion impact energy in the formation of the surface pattern. In Fig. 6g–i we show the dependence of the surface morphology of the Cu(110) surface on ion energy, for fixed $f = 1$ ML/min and T = 230 K. As already observed in Fig. 3 and 5, the LTR state transforms into the RP pattern when decreasing the energy from $\varepsilon = 600$ eV (Fig. 6g) to $\varepsilon = 400$ eV (Fig. 6h), whereas a further decrease of the impact energy down to 200 eV allows to revert the surface morphology into an HTR pattern (Fig. 6i). The sequence of Fig. 6g–i is consistent with the sequence of panels Fig. 6d–f, suggesting that an *increase of the ion flux f* is equivalent to an *increase*

of the ion energy ε. Such behavior can be rationalised if we recall that both STM experiments [25] and molecular dynamics simulations of a single ion impact [26] show a monotonic increase of the adatom production yields when the impact energy is increased in the range 0.1–10 keV. Therefore an increase of the *average* production rate of adatoms can be achieved either through an *increase of* ε (which affects the number of adatoms produced per impact event) or through an *increase of f* (which modifies the rate of single ion impact events). This picture is fairly compatible with the atomistic discussion on Fig. 5 according to which the role of the energy can be regarded as that of the deposition flux, i.e. as source of mobile defects.

Furthermore, from the data in Fig. 5 and 6g–i, we can also conclude that the impact energy affects the formation process of the RP state not through a selective anisotropic etching of the surface, but by controlling the total number of adatoms emitted per collision event which constitute the mobile species that enter the destabilizing massive transport at the base of the self-diffusion in fcc(110) terminated metal surfaces.

Theory: the continuum model

The diffusion of the mobile species can be treated in a unified scheme both under erosion as well as growth conditions by considering a non-equilibrium, tilt-dependent flux of defects $\mathbf{J_{up}}$ as responsible for the surface instability which gives rise to the pattern formation. In a continuum approach, the evolution of the surface profile $h(x,y,t)$ obeys the conservation law $\partial_t h = -\nabla \mathbf{J} + \boldsymbol{\eta}$ described in terms of the total adatom current density $\mathbf{J} = \mathbf{J_{sd}} + \mathbf{J_{up}}(\mathbf{m})$, $\mathbf{J_{sd}}$ being the curvature dependent surface diffusion term (vanishing in flat regions such as facets) and $\mathbf{J_{up}}(\mathbf{m})$ the destabilising contribution which depends on the local slope vector $\mathbf{m} = \nabla \boldsymbol{h}$ and biases diffusion uphill, towards ascending step edges [29]; $\eta(x,y,t)$ accounts for the randomness of the adatom (ion) arrivals.

Metastable structures are reached whenever steps rearrange by selecting local surface slopes $\mathbf{m^*}$ which minimize the $\mathbf{J_{up}}$ current, i.e. for stable zero solutions of $\mathbf{J_{up}}$ [29, 30]. Following Ref. [23, 31], the arrangement of each surface pattern is dictated by the vectorial character of the $\mathbf{m^*}$ solutions. In more detail, non-equivalent pairs of doublet-like solutions ($\mathbf{m^*} = (\pm m_1, 0)$ or $(0, \pm m_2)$) identify two kinds of rippled structures, i.e. the LTR and the HTR pattern, depending on whether the faceting (and the periodicity) is extended along the $\langle 1-10 \rangle$ or the $\langle 001 \rangle$ direction, respectively [32]. The coexistence of both pairs of doublet-like solutions ($\mathbf{m^*} = (\pm m_1, 0)$ and $(0, \pm m_2)$) expresses the occurrence of rectangular faceting which identifies the RM pattern. Quartet-like solutions of the form $\mathbf{m^*} = (\pm m_1, \pm m_2)$ reflect the presence of 2D pyramid structures having a

rhomboidal shaped contour lines formed by step-edges (the RP state). Consecutive transitions among these surface configurations can be achieved upon variation of the intrinsic details of the $\mathbf{J_{up}}$ current as results in the morphological phase diagram of Fig. 7a obtained from a continuum approach to the surface evolution under erosion [23, 31]. It is also interesting to stress how the same theoretical study allows to single out the formation of surface patterns with structural arrangements similar to those observed in our experiments. For instance, surface models elaborated in Fig. 7b discriminate a universal rippled state from peculiar RP pattern and from a RM pattern. The strong similarity between the nanopatterning of the Rh(110) and the Cu(110) surfaces suggests that the predictions of the continuum approach and the consecutive morphological transformations can be extended to a broader class of unreconstructed fcc(110) substrates. Finally, the observation of the scaling law of the lateral correlation and of the interface width (rms roughness) of the rhomboidal pyramids and of the LTR ripples as a function of the irradiation dose (Fig. 8a and 8b) provides a good agreement with the predictions of the continuum models of Ref. [23, 31] further reinforcing the assignments made. Additionally the data shown in Fig. 8 demonstrate that it is possible to tune the separation of the nanopyramids and of the LTR ripples as well as their roughness within significant range, which provides a valuable tool for tuning their morphological properties in view of applications.

Chemical reactivity

We have studied CO interaction with the Rh nanostructured surfaces described in Sect. 2.1 by using High-Energy Resolution Core Level Spectroscopy with synchrotron radiation, to probe the coverage evolution and the molecular dissociation process. The photoemission studies were performed at the SuperESCA beamline [33, 34] of the Elettra third generation synchrotron radiation source in Trieste, Italy. The experimental chamber is equipped with a double pass hemispherical electron energy analyser with 96 channels detector [35]. During the measurements the background pressure in the main chamber was always better than 2×10^{-10} mbar. The Rh(110) single crystal was cleaned by Xe ion sputtering at room temperature (E = 1 keV), flash to 1300 K, oxygen cycles in order to remove residual carbon (in the range 570–1070 K at $P_{O2} = 5 \times 10^{-8}$ mbar) and finally, hydrogen reduction to remove residual oxygen traces ($P_{H2} = 1 \times 10^{-7}$ mbar, T = 470–770 K). Surface cleanliness prior to nanostructures preparation was checked by measuring C1s, S2p and O1s signals. C1s and O1s spectra were recorded always at a sample temperature of 200 K in order to reduce temperature broadening of the
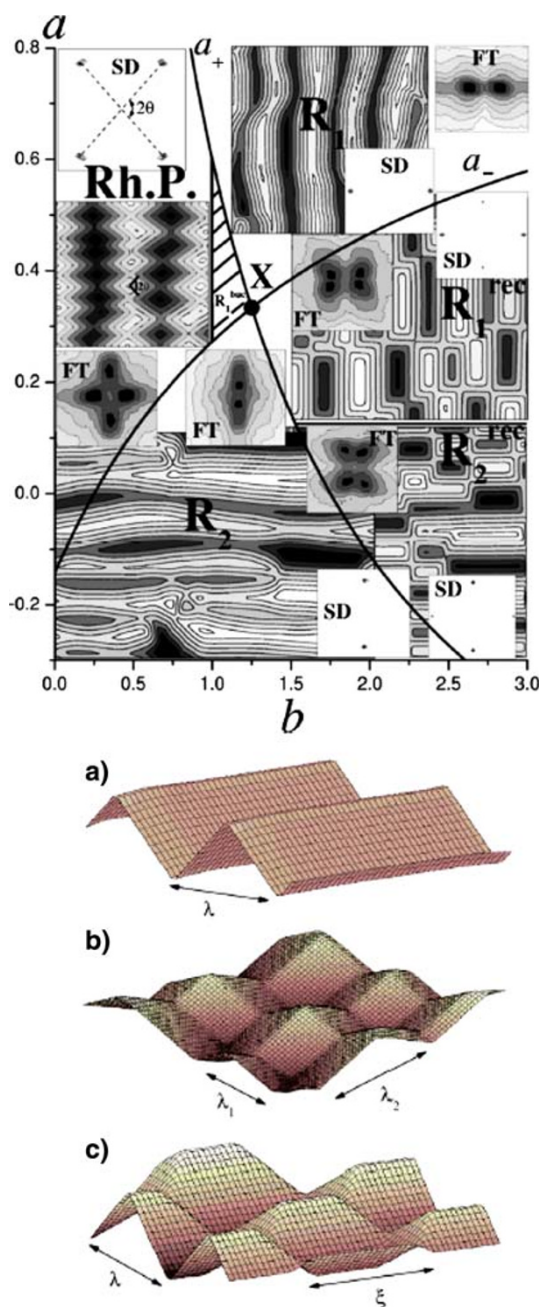
Fig. 8 Evolution of the correlation length $\Lambda_{<1-10>}$ through the $<1-10>$ direction (**a**) and of the estimated surface roughness W_{est} (**b**) for the RP and LTR surface patterns at different fluences. In panel (**a**) the scaling behavior of the LTR wavelength is also reported. The figure is reproduced from Ref. [18]

Fig. 7 (**a**) Kinetic phase diagram depicting various interfacial states in terms of their basic properties (as obtained from simulations of ref. [31]): surface contour plots, magnitudes of interfacial height Fourier transforms (FT), corresponding to near in-phase diffraction patterns, and slope distributions (SD) in the *slope* space, corresponding to out-of-phase diffraction patterns. R_1 and R_2 are the two rippled states, RhP is the rhomboidal pyramid state, R_1^{rec} and R_2^{rec} are the two rectangular rippled states, and R_1^{buc} (hatched domain) is the buckled rippled . See Ref. [31] for details. (**b**) Three-dimensional (3D) views of various interfacial states from the simulations of Ref. [31]: (**a**) rippled state with the period λ, (**b**) rhomboidal pyramid state with the periods λ_1 and λ_2, and (**c**) rectangular rippled state, with the period λ, which motif is a rooflike pyramid (hut), with a long rooftop edge of the length ξ. The figures are reproduced from Ref. [31]
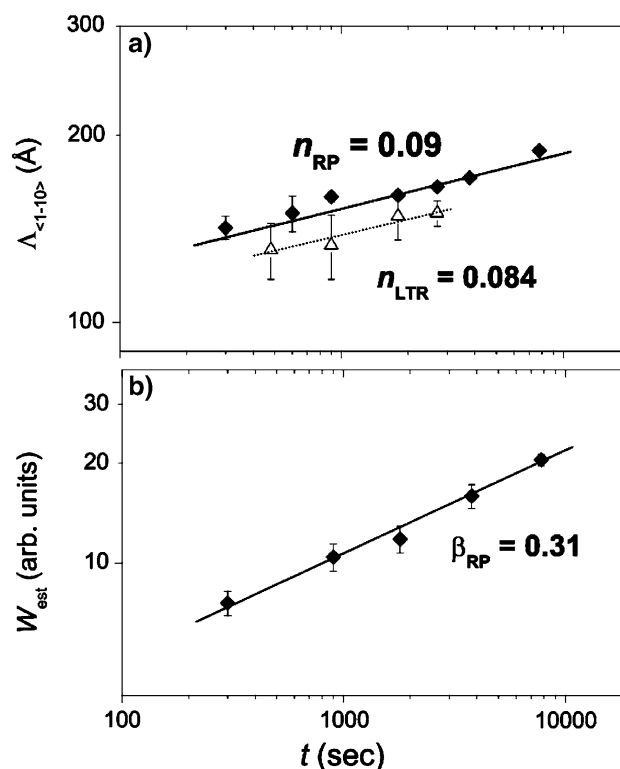
peaks and in normal emission conditions. Photon energies of 400 and 650 eV were used for C1s and O1s spectra, with an overall energy resolution (X-ray monochromator and electron energy analyser) of 150 and 300 meV, respectively. In these conditions typical data acquisition time was 5 min/spectrum. Core level spectra binding energies have always been calibrated with respect to the Fermi level.

The XPS analysis was done by fitting the core level spectra with a Doniach-Šunjić (DS) function [36], characterized by two parameters: the singularity index α (describing the asymmetry of the core level spectra due to electron–hole pairs excitations) and the Lorentzian width Γ (because of the natural core-hole lifetime), convoluted with a Gaussian, which takes into account the broadening due to unresolved vibrations, many-body effects and the instrumental resolution. A linear background was also included in the fit.

Chemical reactivity: experimental results on RP

It is well established that both oxygen and carbon 1s core-level signals are strongly sensitive to the local molecular and atomic adsorption sites, and can be used to determine

the CO adsorption geometry. In particular, for a large number of carbon monoxide adsorption systems it was found that the binding energy (BE) decreases with increasing CO coordination to the substrate atoms, i.e. in the order BE(on-top) > BE(bridge) > BE(hollow), with a shift which is about twice as large for O1s than for C1s [37]. The O1s BE on different TM single-crystal surfaces varies in the range 531.6–532.6 eV for on-top bonded CO and between 530.5 and 531.6 eV for bridge-bonded CO [38]. The reason of this trend can be understood from total energy considerations, the major contribution to the shift originating from the changes in the energy of the core ionized final state. Indeed the difference of the CO adsorption energies between different adsorption sites for the neutral initial state is very small (~100 meV) [37]. Carbon and oxygen atomic species when chemisorbed on transition metal surfaces, usually produce core level components at lower BE. In particular carbon species are found at about 284 eV, while chemisorbed oxygen at about 530 eV.

The CO adsorption and the temperature evolution of the chemisorbed layer have been measured for HTR, LTR and RP nanostructures, produced using the procedures reported above.

The growth of the RP nanostructures was characterized in situ by low energy electron diffraction (LEED). The appearance of a fourfold splitting of the (00) diffraction peak along diagonal directions demonstrates the formation of the RP facets. The diffraction pattern is in agreement with the SPA-LEED results reported in Fig. 4. Carbon monoxide was firstly dosed on the Rh(110) nanostructured surface at T = 200 K, i.e. well before the CO desorption onset on the clean (1 × 1) Rh(110) surface [39–41], at different initial coverage, ranging from ~0.03 ML for the RP to saturation.

As for the (111), (100) and (110) Rh surfaces, CO adsorption on RPs at saturation (Fig. 9) leads to the occupation of two different adsorption sites. By analogy with the (110) flat surface [41], the higher BE C1s (Fig. 9a)

and O1s (Fig. 9b) components, at 286 and 531.7 eV respectively, are assigned to molecules sitting in on-top sites, while the lower BE peaks, to CO placed in bridge sites (BE of 285.55 and 530.5 eV). The spectra reported in Fig. 9 show that, for both signals, the Gaussian width of the on-top component is always larger than that of the bridge-bonded CO. Besides the presence of unresolved vibrational excitations [40, 42], this behavior can be explained in terms of occupation of local inequivalent on-top configurations. Indeed the small terraces present on the RPs can be occupied by CO sitting just below or above the steps (T_A and T_C sites in Fig. 9c) or in the terrace (T_B site). At the contrary the Gaussian width of C1s and O1s signals relative to bridge-bonded CO is much lower and this can be tentatively interpreted as due to single site occupation.

Figures 10 and 11 show the evolution of the C1s and O1s spectra after annealing of the CO saturated layer, which evidence the different behavior of the two CO bonding configurations, as well as the onset of CO dissociation. The two CO related components behave similarly in the C1s and O1s regions. The C1s spectra drastically change with increasing the annealing temperature: they lose intensity due to CO desorption while the ratio on-top to bridge population clearly increases with increasing the temperature. This behavior parallels that observed on the flat (110) surface using Temperature Programmed XPS where a conversion from bridge to on-top sites takes place during heating [41].

The evolution of the intensity of the C1s components is reported in Fig. 12. The relative intensities have been rescaled because of photoelectron diffraction effects which are known to be relevant at this photoelectron kinetic energies. In order to do this, high energy spectra (E_{kin} > 250 eV) have been acquired. This is the reason also of the different on-top to bridge bonded CO population observed in the O1s experiments. Up to about 450 K the decrease of the total CO coverage is mainly dominated by

Fig. 9 (**a**) C1s and (**b**) O1s core-level spectra showing the components corresponding to molecular CO adsorbed at saturation on the Rh nano-pyramids. (**c**) Possibile inequivalent on-top (T_A,T_B,T_C) and bridge (B_A, B_B) adsorption sites are indicated
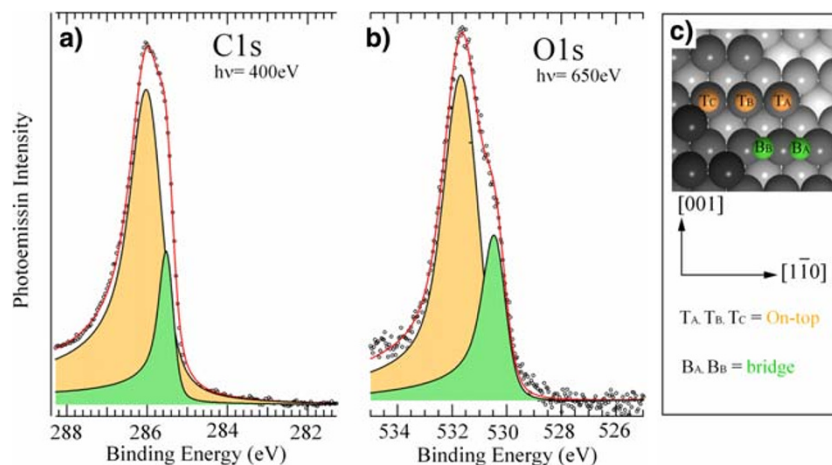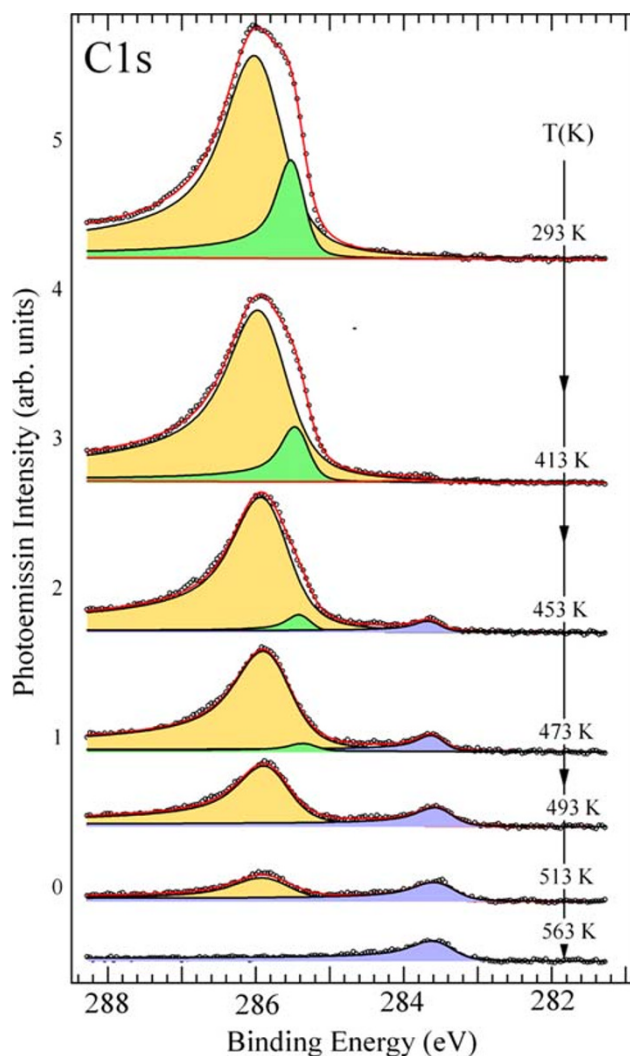
Fig. 10 Evolution of the C1s core level spectra after annealing of the CO saturated layer prepared on the Rhomboidal Pyramids at different temperatures and quenching at 250 K. The peak at 286 and 285.55 eV correspond to CO in on-top (orange) and bridge (green) sites, respectively. The component at 283.55 eV (blue) is due to atomic carbon. $h\nu = 400$ eV

Fig. 11 Evolution of the O1s core level spectra after annealing of the CO saturated layer prepared on the Rhomboidal Pyramids at different temperatures and quenching at 250 K. The peak at 531.7 and 530.5 eV correspond to CO in on-top (orange) and bridge (green) sites, respectively. The component at ~530 eV (blue) is due to atomic oxygen. $h\nu = 650$ eV

the CO bridge-bonded depopulation. The changes in the relative population of the on-top and bridge sites is in agreement with the predominant occupation of on-top sites at CO coverage > 0.3 ML. The shift to lower binding energy of the on-top component with increasing the annealing temperature ($\Delta E = -80$ meV) can be explained in different ways: (i) preferential occupation of one of the three available on-top adsorption sites (see Fig. 9c), (ii) changes of interatomic molecular interactions between CO molecules at different coverage or (iii) partial occupation of three-fold sites in the (111) facets of the nano-pyramids.

However, the most interesting result of the heating process is that not all the CO desorbs but a minor fraction converts into atomic species already at ~450 K, as evi-
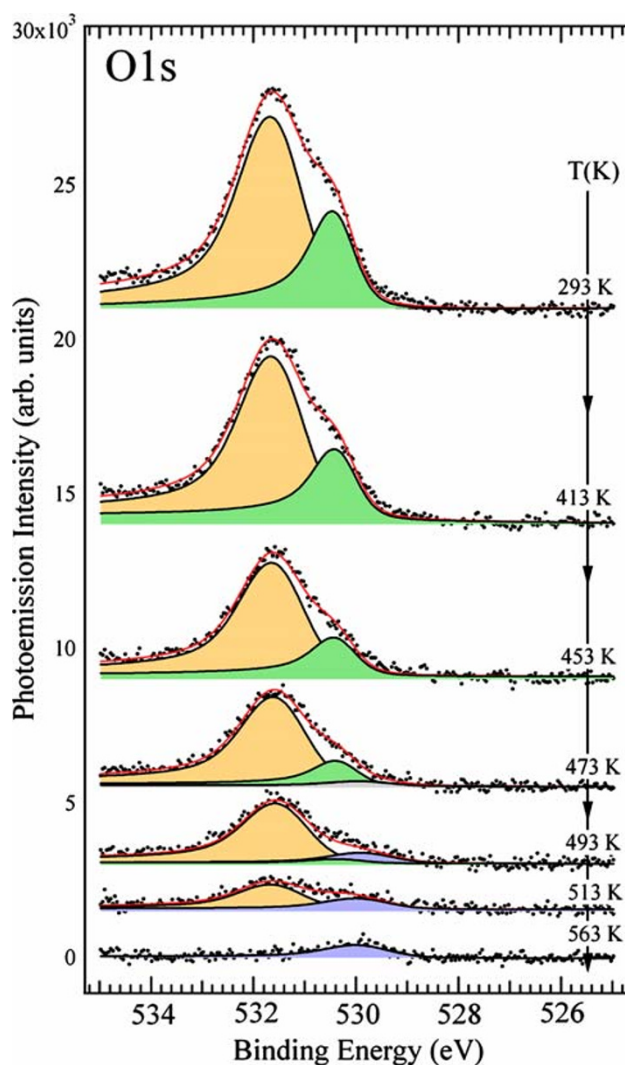
denced by the increase of lower binding energy components in both, C1s (283.55 eV) and O1s spectra (~530 eV). Indeed, after the removal of bridge-bonded CO, the on-top sites are gradually depopulated and the surface remains completely free of CO for T > 525 K. After heating to 563 K, 9.4 ± 0.5% of the initial CO has converted into atomic carbon. O1s spectra show the presence of a residual amount of atomic oxygen. Atomic oxygen species are expected to desorb as molecular oxygen at temperatures higher than 750 K. The lower amount of atomic oxygen is therefore interpreted as due to the CO + O → CO$_2$ reaction followed by CO$_2$ desorption [43].

The heating experiment has been repeated with a lower CO coverage (0.21 ML) adsorbed on the RP at 200 K
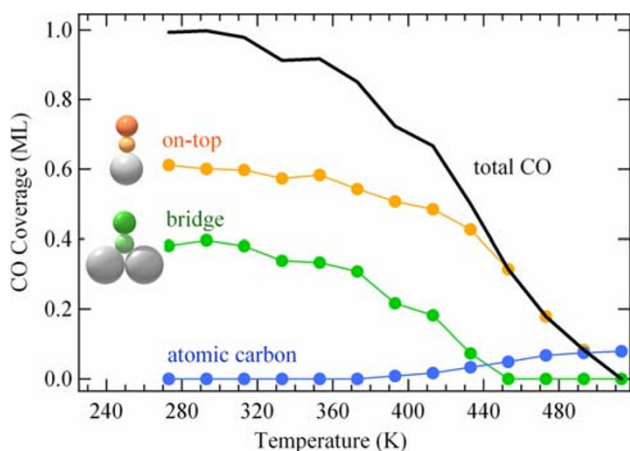
Fig. 12 Plot of the normalized C1s intensity versus annealing temperature for a CO saturated layer prepared on the Rhomboidal Pyramids at T = 200 K relative to the overall CO coverage (black curve) and to CO species in on-top (orange) and bridge (green) sites. Atomic carbon is shown in blue

(Fig. 13). In this case the initial layer is formed mainly by CO molecules sitting in on-top sites with a residual population of bridge-bonded molecules (see Fig. 13a top spectrum). We observe a similar temperature behavior of the surface population, with the bridge-bonded CO molecules disappearing before the on-top moieties and the atomic carbon species increasing already at temperatures above 370 K. We interpret the increase of carbon as due to CO dissociation in on-top sites. In this case the fraction of dissociated CO after annealing at 563 K represent 22 ± 3% of the total CO initial intensity, i.e. much larger than the value obtained for the CO saturated layer.

The increase of CO dissociation probability on RP with decreasing the initial CO coverage is unambiguously confirmed by the temperature behavior of a very low CO coverage layer (0.03 ML) adsorbed at 200 K (Fig. 13b). In this case 80 ± 14% of the CO molecules adsorbed in on-top sites undergo dissociation.

Chemical reactivity: experimental results on HT and LT Ripples

The large set of inequivalent Rh nanostructured surfaces prepared under different experimental conditions, allowed us to investigate the CO dissociation process also on HTR structures.

Figure 14 shows the temperature evolution of the C1s spectra after CO adsorption at 200 K on the HTR structures and Fig. 15 shows the behavior of the intensity of the different C1s components. As for the RP case, the low temperature spectra can be analyzed by using two fitting components, corresponding to CO in on-top and bridge sites. The saturation coverage is very similar to the RP
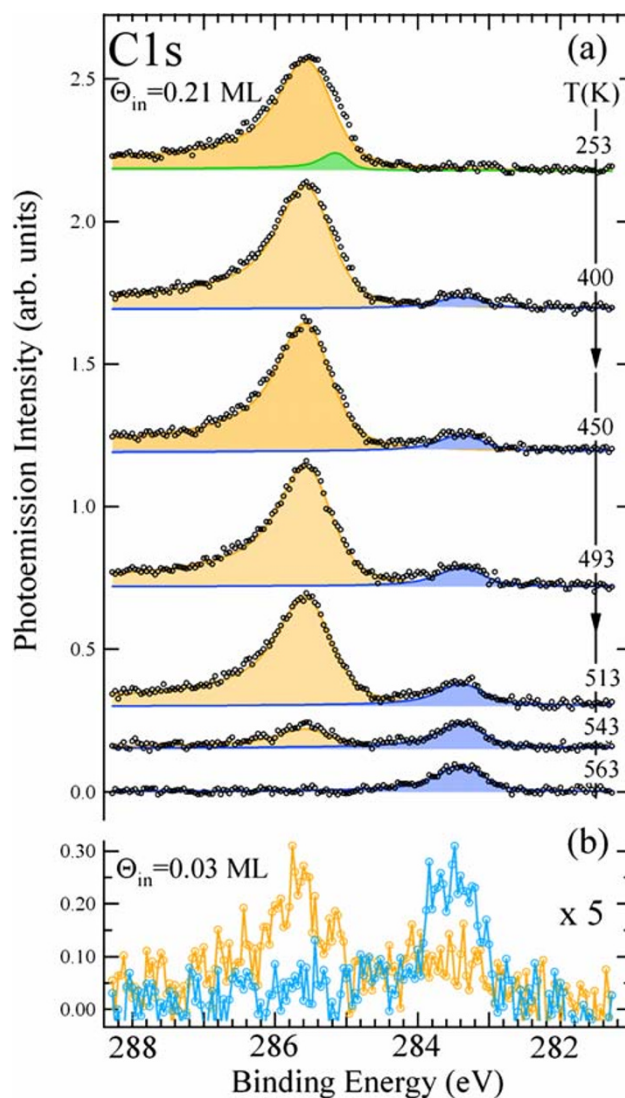

Fig. 13 (a) Evolution of the C1s core level spectra after annealing at different temperatures of the 0.21 ML CO layer prepared on the Rhomboidal Pyramids and quenching at 250 K. (b) Same as in (a) but with a very small initial CO coverage (Θ = 0.03 ML) hν = 400 eV

case, being only 8% larger. For the HTR the normalized top/bridge intensity ratio is slightly smaller, indicating a higher tendency to form CO bridge bonds with the Rh substrate. Up to 350 K the overall CO coverage is almost constant, as is the ratio of on-top to bridge CO populations. CO desorption starts at T > 350 K, while atomic carbon formation takes place only at 475 K. The onset of CO dissociation on the HTR is therefore shifted by about 85 K to higher temperature, compared to CO on the RP nanostructures (T = 375 K). Our results show that for the HTR only 4.2% of the initial CO population converts into atomic carbon, while the rest of CO molecules desorb. The same experiment performed on the LTR nanostructures shows a similar behavior, with the onset of CO dissociation shifted
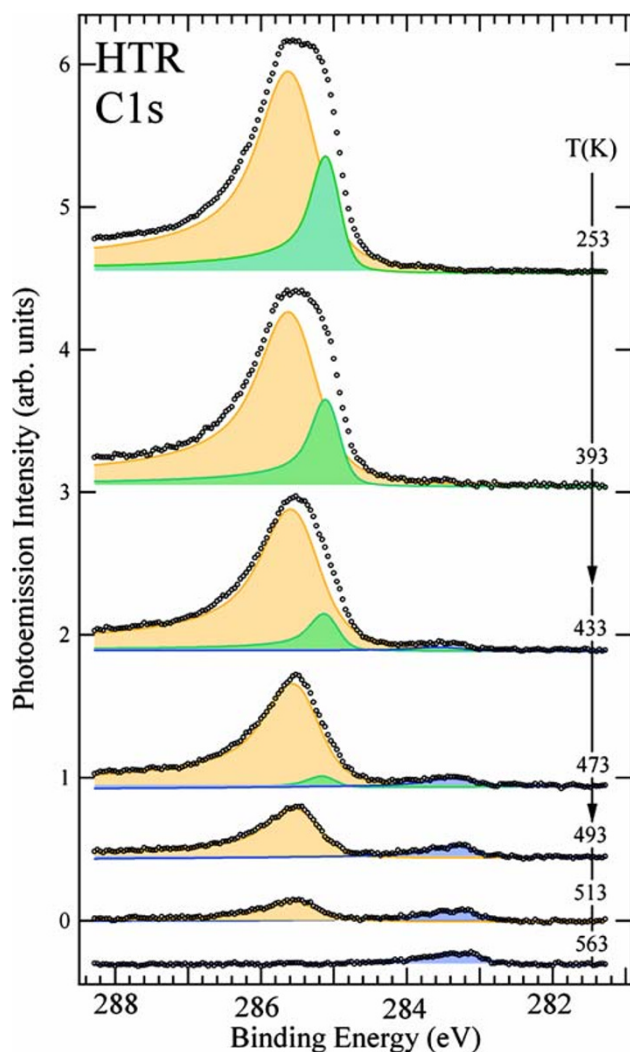
Fig. 14 Evolution of the C1s core level spectra after annealing at different temperatures of the CO saturated layer prepared on the High Temperature Ripples and quenching at 250 K. The peak at 286 and 285.55 eV correspond to CO in on-top (orange) and bridge (green) sites, respectively. The component at 283.55 eV (blue) is due to atomic carbon. $h\nu$ = 400 eV

Fig. 15 Plot of the normalized C1s intensity versus annealing temperature for a CO saturated layer prepared on the High Temperature Ripples at T = 200 K relative to the overall CO coverage (black curve) and to CO species in on-top (orange) and bridge (green) sites. Atomic carbon is shown in blue

at even higher temperatures with only 3.8% of the CO saturated layer undergoing dissociation.

The same annealing experiments have been performed after CO saturation of the (1 × 1) Rh(110) in order to make a detailed comparison with the nanostructured surfaces. We find evidence that in this condition only 2.4% of CO undergoes dissociation. This result can be explained as due to a residual density of surface defects on the (1 × 1) substrate. Indeed, even on a well prepared surface with a typical miscut of 0.2°, about 1% of the surface atoms reside at the steps.

Chemical reactivity: discussion

Among the factors that govern the Rh surface reactivity, the density of under-coordinated atoms involved in the
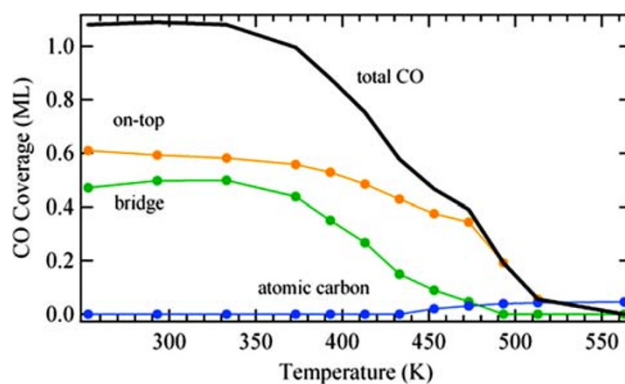
reaction plays a very important role. In order to compare the CO dissociation behavior on Rh nanostructured surfaces with that on other Rh crystallographic planes, we have to consider the different atomic coordination on Rh nanostructures. At variance with the (111), (100) and (110) flat Rh surfaces, which present first layer atoms with coordination 9, 8 and 7 respectively, the nanopyramids are composed by a large number of under-coordinated atoms, as shown in Fig. 16a.

Aiming at a comparison in surface reactivity between different nanostructured surfaces we firstly evaluate the density of under-coordinated surface atoms on RP. Figure 16a shows the local model structure of the top of a RP: it is evident that, together with a small amount of Rh atoms with coordination $n = 5$ (n = number of nearest neighbors) (yellow atoms in Fig. 16), there is a large number of atoms with coordination 6 (orange). These are the atoms either forming the steps oriented along the [1–12] direction or sitting at the top of the nano-pyramid. Also the LTR and the HTR nanostructures, reported in Fig. 16b and c are formed by a considerable amount of 6-fold coordinated atoms. However the main difference among these structures resides in the next-nearest (l) neighbors. In Table 1 we have estimated the density of local atomic configurations for the different morphologies that we have produced. The typical average dimension of the RP clusters are 15 nm along the [1–10] direction, corresponding to an average number of 12 exposed layers. The data have been reported according to the number n_l of nearest (n) and next-nearest (l) neighbors. What appears peculiar to the RP, with respect to the LTR and HTR morphology, is the very high density of kinked microfacets, produced by the steps running along [1–12], which provide a high density of low-coordinated atoms labeled (6) in Fig. 16. The local atomic configuration of the RP microfacets represents an *open*
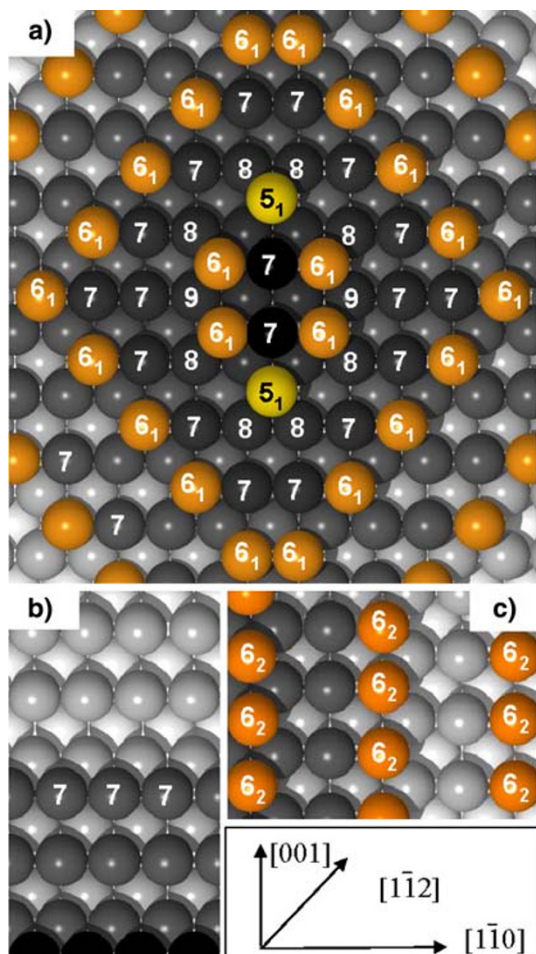
Fig. 16 Model for Rhomboidal Pyramids (**a**) determined from the SPA-LEED data and for the High Temperature Ripples (**b**) and Low Temperature Ripples (**c**). Atomic coordination n_l are also reported, with n = number of nearest neighbors and l = number of next-nearest neighbors

densities between 3% and 34%, respectively), increases, thus resulting in a higher fraction of dissociated CO. We expect that the activation energy for CO dissociation on these sites can be even lower than on the Rh(211) steps ($n = 7$) or kinks ($n = 6$) for which calculations [11] have found activation energies of 0.30 and 0.21 eV, respectively.

Another interesting feature of our experimental results is the increased CO dissociation rate with smaller initial CO coverage on the RP. This can be correlated with the increased availability of undercoordinated atoms, with CO occupying on-top sites at the steps, i.e. the most probable adsorption site. The on-top CO adsorption geometries on the small (110) microterraces and steps can be very similar, but we expect that, as for the (211) stepped surface [12], CO is more stable at the steps. We associate this with the fact that the Rh 4d electrons are higher in energy and thus interact more strongly with the CO valence states as for CO on Rh stepped surfaces. With increasing the CO coverage only a residual amount of CO molecules can stay on the atoms at the steps. Moreover, the fact that also the adsorbed C and O strongly bind to the steps indicates that during the annealing experiment the products can poison the active sites and we expect that the reaction should stop when all step sites are occupied.

The increased chemical reactivity on nanoparticle catalysts supported on surface oxide is also connected to the presence of special defect configurations. This has been observed in core-level photoemission experiments on alumina-supported Rh particles as a function of particle size [15, 16]. The maximum dissociation rate of 50% was found for particles containing about 1000 Rh atoms, with the reactivity decreasing for larger clusters. The RP clusters produced in our experiments, formed by ~3000 atoms, result in a dissociation fraction ranging from 10% up to 80%, which nicely compares with the 30% of Rh nanoclusters of similar dimension. These findings suggest that the role of the support in CO dissociation is marginal and that chemical reactivity is mainly governed by the density of undercoordinated surface atoms.

morphology [the nearest neighbor number n is 6 with only 1 next n.n. ($l = 1$)], with an increase of $\approx 73\%$ of the distance between Rh atoms along the steps compared to the nearest neighbor distance of bulk Rh. Indeed, with decreasing the initial CO coverage the availability of 6_1 Rh atoms, with CO sitting in on-top sites (estimated surface

Table 1 Occupancy (in %) of the different sites labeled n_l, according to the number of nearest n and next-nearest neighbors l for the different nanostructures (RP, HTR and LTR) and for the (110) flat terraces. The sites can be identified in the following way: 5_1 = upper step corner atom, 6_1 = upper step (100) facet, 7_1 = upper step (111) facet, 7_2 = (110) terrace atoms, 8_1 = lower step RP facets, 9_2 = lower step (111) facets, 9_2 = lower step (100) facets

Site	5_1	6_1	6_2	7_1	7_1	8_1	9_2	9_2
RP	2.8	33.9			35.8	23.9	1.8	1.8
HTR				33	33			33
LTR			33		33			33
Terrace					100			

Conclusions

The growth of out-of-equilibrium morphological structures formed during Xenon ion irradiation on Rh(110) substrate is reported. The formation of rhomboydal pyramids and the transition to high temperature and low temperture ripple phases result from the interplay between different kinetic processes depending on temperature, flux and impact energy. Our results illustrate the close correlation between dissociation probability and surface morphology of nano-structured surfaces, a fundamental issue in surface chemistry and nano-catalysis. The RP strongly increase the CO dissociation probability because of the high density of under-coordinated Rh atoms. Detailed comparison of dissociation probability of different nanostructured surfaces shows that CO dissociation takes place in on-top configuration at the kinked step edges. This study shows that it is possibile to change in a controlled way the catalytic properties by changing the density of low coordinated atoms on nanostructured surfaces.

References

1. R. Moroni, D. Sekiba, F. Buatier de Mongeot, G. Gonella, C. Boragno, L. Mattera, U. Valbusa, Phys. Rev. Lett. **91**, 167207 (2003)
2. A. Crucq (ed.), *Catalysis and Automotive Pollution Control II, Studies in Surface Science and Catalysis*, vol. 71. (Elsevier, Amsterdam, 1991)
3. D.S. Newsome, Cat. Rev.-Sci. Eng **21**, 275 (1980)
4. Y. Zhang, G. Jacobs, D.E. Sparks, M.E. Dry, B.H. Davis, Catal. Today **71**, 411 (2002)
5. G.A. Somorjai, *Introduction to Surface Chemistry and Catalysis* (Wiley, New York, 1994)
6. T. Zubkov, G.A. Morgan, J.T. Yates, O. Kuhlert, M. Lisowski, R. Schillinger, D. Fick, H.J. Jansch, Surf. Sci. **526**, 57 (2003)
7. T. Zubkov, G.A. Morgan, Jr., J.T. Yates, Jr., Chem. Phys. Lett. **362**, 181 (2002)
8. B. Hammer, J.K. Nørskov, Surf. Sci. **343**, 211 (1995)
9. B. Hammer, O.H. Nielsen, J.K. Nørskov, Catal. Lett. **46**, 31 (1997)
10. S. Dahl, A. Logadottier, R.C. Egeberg, J.H. Larsen, I. Chorkendorff, E. Tornqvist, J.K. Nørskov, Phys. Rev. Lett. **83**, 1814 (1999)
11. Z.-P. Liu, P. Hu, J. Am. Chem. Soc. **125**, 1958 (2003)
12. M. Mavrikakis, M. Bäumer, H.-J. Freund, J.K. Nørskov, Catal. Lett. **81**, 153 (2002)
13. J.C. Campuzano, in *The Chemical Physics of Solid Surfaces and Heterogeneous Catalysis*, ed. by D.A. King, D.P. Woodruff (Elsevier, New York 1990), vol. 3, p. 389
14. M. Rebholz, R. Prins, N. Kruse, Surf. Sci. **259**, L797 (1991)
15. S. Andersson, M. Frank, A. Sandell, A. Giertz, B. Brena, P.A. Bruhwiler, N. Martensson, J. Libuda, M. Baumer, H.-J. Freund, J. Chem. Phys. **108**, 2967 (1998)
16. G. Ertl, H.-J. Freund, Phys. Today **52**, 32 (1999)
17. A. Molle, F. Buatier de Mongeot, A. Molinari, F. Fuerkaiti, C. Boragno and U. Valbusa, Phys. Rev. Lett. **93**, 256103 (2004)
18. A. Molle, F. Buatier de Mongeot, A. Molinari, C. Boragno, U. Valbusa, Phys. Rev. B **73**, 155418 (2006)
19. S. Rusponi, G. Costantini, F. Buatier de Mongeot, C. Boragno, U. Valbusa, Appl. Phys. Lett. 75: 3318 (1999)
20. F. Buatier de Mongeot, G. Costantini, C. Boragno, U. Valbusa, Phys. Rev. Lett. **84**, 2445 (2000)
21. S. Rusponi, C. Boragno, U. Valbusa, Phys. Rev. Lett. **78**, 2795 (1997)
22. Rusponi S., Costantini G., Boragno C., Valbusa U. Phys. Rev. Lett. 81735 (1998)
23. L. Golubovic', A. Levandovsky, D. Moldovan, Phys. Rev. Lett. **89**, 266104 (2002)
24. G. Costantini, F. Buatier de Mongeot, C. Boragno, U. Valbusa, Phys. Rev. Lett. **86**, 838 (2000)
25. Th. Michely, C. Teichert, Phys. Rev. B **50**, 11156 (1994)
26. E.M. Bringa, K. Nordlund, J. Keinonen, Phys. Rev. B **64**, 235426 (2001)
27. S. van Dijken, D. de Bruin, B. Poelsema, Phys. Rev. Lett. **86**, 4608 (2000)
28. M. Ghaly, R.S. Averback, Phys. Rev. Lett. **72**, 364 (1994)
29. J. Villain, J. Phys. 1 (France) **1**, 19 (1991)
30. M. Siegert and Plischke, Phys. Rev. Lett. **73**, 1517 (1994)
31. A. Levandovsky, L. Golubović, D. Moldovan, Phys. Rev. E **74**, 061601 (2007)
32. C. Boragno, F. Buatier de Mongeot, G. Costantini, A. Molle, D. De Sanctis, U. Valbusa, R. Felici, S. Ferrer, Phys. Rev. B **68**, 094102 (2003)
33. A. Baraldi, M. Barnaba, B. Brena, D. Cocco, G. Comelli, S. Lizzit, G. Paolucci, R. Rosei, J. Electron Spectrosc. Relat. Phenom. **76**, 145 (1995)
34. A. Baraldi, G. Comelli, S. Lizzit, M. Kiskinova, G. Paolucci, Surf. Sci. Rep. **49**, 169 (2003)
35. A. Baraldi, V.R. Dhanak, J. Electron Spectrosc. Relat. Phenom. **67**, 211 (1994)
36. S. Doniach, M. Šunjić, J. Phys. C **3**, 185 (1970)
37. N. Mårtensson, A. Nilsson, in *Springer Series in Surface Science*, ed. by W. Eberhardt (Springer-Verlag, Berlin, 1994), vol. 35
38. V.R. Dhanak, A. Baraldi, G. Comelli, G. Paolucci, M. Kiskinova, R. Rosei, Surf. Sci. **295**, 287 (1993)
39. A. Baraldi, V.R. Dhanak, G. Comelli, K.C. Prince, R. Rosei, Surf. Sci. **293**, 246 (1993)
40. V.R. Dhanak, A. Baraldi, G. Comelli, G. Paolucci, M. Kiskinova, R. Rosei, Surf. Sci. **295**, 287 (1993)
41. A. Baraldi, G. Comelli, S. Lizzit, D. Cocco, G. Paolucci, R. Rosei, Surf. Sci. **367**, L67 (1996)
42. M. Smedh, A. Beutler, T. Ramsvik, R. Nyholm, M. Borg, J.N. Andersen, R. Duschek, M. Sock, F.P. Netzer, M.G. Ramsey, Surf. Sci. **491**, 99 (2001)
43. A. Baraldi, S. Lizzit, D. Cocco, G. Comelli, G. Paolucci, R. Rosei, M. Kiskinova, Surf. Sci. **385**, 376 (1997)